The magneto-transport properties of $Cr_{1/3}TaS_2$ with chiral magnetic solitons

*Dimuthu Obeysekera, Kasun Gamage, Yunpeng Gao, Sang-wook Cheong, Junjie Yang**

Dimuthu Obeysekera, Yunpeng Gao, Junjie Yang

Department of Physics, New Jersey Institute of Technology, NJ 07102, USA

Email Address: jyang@njit.edu

Kasun Gamage

Department of Physics, Central Michigan University, Mount Pleasant, MI 48858, USA

Sang-wook Cheong

Rutgers Center for Emergent Materials and Department of Physics and Astronomy, Piscataway, NJ 08854, USA

Keywords: chiral magnet, single crystal growth, magnetic phase diagram, magnetoresistance

$Cr_{1/3}TaS_2$ – a candidate of chiral magnet – has been reported as a trivial ferromagnetic material. In contrast, our $Cr_{1/3}TaS_2$ single crystals exhibit a chiral helimagnetic (CHM) transition near 140 K. The magnetic moment vs magnetic field curves reveal a CHM – chiral soliton lattice (CSL) – forced ferromagnetic (FFM) transition in the magnetic ordered state. The conducting electrons interact with the CHM and CSL orders, giving rise to the nontrivial magnetoresistance (*MR*) in our $Cr_{1/3}TaS_2$ single crystals. The normalized magnetic moment and normalized *MR* fit well with the analytical functions for chiral soliton density. The magnetic phase diagrams constructed from the magnetic moment data

and *MR* data suggest a possible tri-critical point. Compared with the isostructural $Cr_{1/3}NbS_2$, the CHM transition temperature of $Cr_{1/3}TaS_2$ is 13 K higher, the CSL – FFM transition field is about 10 times larger, and the Dzyaloshinskii-Moriya interaction strength is 3 times bigger. The latter two likely originate from the strong spin-orbit coupling (SOC) of $Cr_{1/3}TaS_2$. Our work clarifies that high-quality $Cr_{1/3}TaS_2$ single crystals are chiral magnets and $Cr_{1/3}(Nb,Ta)S_2$ could serve as an intriguing platform for the flexible engineering of chiral magnetic solitons with tunable SOC.

1. INTRODUCTION

Chiral magnets have attracted much attention because of their exotic physics and potential applications in the next generation of electronics.[1–7] Particularly, chiral magnetic nanostructures, e. g., chiral soliton lattice (CSL), have been observed in chiral magnets.[1–4] It has been proposed that the chiral magnetic solitons in metallic chiral magnets can be manipulated by spin polarized current and used for fast logical operations.[8–10] Compared with the domain wall motion in a ferromagnetic nanowire, the chiral soliton motion could reach a much larger velocity at a much smaller current density.[9,11] The metallic chiral magnets that can host CSL are very rare. As far as we know, the formation of CSL in metallic chiral magnets has been only observed in $Cr_{1/3}NbS_2$ and $YbNi_3Al_9$.[2,3,12,13] As the stability of chiral magnetic solitons is determined by the Dzyaloshinskii-Moriya (*DM*) interaction and the velocity of soliton motion is controlled by the non–adiabatic torque, searching for new chiral magnets associate with strong *DM* interaction and large non–adiabatic torque is of great importance in the emerging field of solitonics.[2,3,8,9] Among the various candidates, the magnetic ion (*M* = Cr, Mn, Fe, Co, and Ni) intercalated $M_{1/3}TaS_2$ stands out because the parent

compound TaS_2 has large spin-orbit coupling (SOC) and hosts a rich collection of exotic states including the Mott state, charge density wave, and quantum spin liquid.[14–16] As the magnetic ions insert into TaS_2, the ordering of magnetic ions in $M_{1/3}TaS_2$ results in a (1/3, 1/3, 0) superstructure with a chiral space group of $P6_322$.[17] The strong SOC and the chiral lattice structure of $M_{1/3}TaS_2$ could induce strong *DM* interaction and large non-adiabatic torque, since the strength of *DM* interaction and non-adiabatic torque both are proportional to the SOC constant.[18,19] In the family of $M_{1/3}TaS_2$, only $Fe_{1/3}TaS_2$ has been confirmed as a chiral magnet.[17,20] Nevertheless, the extremely large orbital magnetic moment of Fe^{2+} ions yields the gigantic easy-axis magnetocrystalline anisotropy and brings on the Ising-type ferromagnetic structure in $Fe_{1/3}TaS_2$.[17,21] The crystal growth and characterization of several other $M_{1/3}TaS_2$ have been studied as early as the 1980s, yet whether the crystals possess chiral lattice structure and chiral magnetism are in question.[22–24] For example, the $Cr_{1/3}TaS_2$ has been reported to exhibit a trivial ferromagnetic (FM) transition near 115 K without any hints of chiral features.[22–25]

In this work, we report the magneto-transport properties and magnetic phase diagrams of $Cr_{1/3}TaS_2$ single crystals. In contrast with the reported trivial FM transition, our $Cr_{1/3}TaS_2$ single crystals exhibit a chiral helimagnetic (CHM) transition near 140 K. The conducting electrons interact with the CHM and CSL orders, giving rise to the nontrivial magnetoresistance (*MR*) in $Cr_{1/3}TaS_2$. The normalized magnetic moment and normalized *MR* fit well with the analytical functions for chiral soliton density derived from the chiral Sine-Gordon Hamiltonian. The magnetic phase diagrams constructed by magnetic moment data and *MR* data confirm the CHM – CSL – forced ferromagnetic (FFM) transition and reveal a possible tri-critical point. Compared with $Cr_{1/3}NbS_2$, the CHM transition temperature (T_{CHM}) of our $Cr_{1/3}TaS_2$ single crystal is 13 K higher, the CSL – FFM transition field of

$Cr_{1/3}TaS_2$ is about 10 times larger, and the extracted *DM* interaction strength D_z is 3 times bigger, indicating more robust CHM and CSL states in $Cr_{1/3}TaS_2$.[26–28] As the strength of *DM* interaction is proportional to the SOC constant, the robustness of CSL state and strong *DM* interaction in $Cr_{1/3}TaS_2$ likely originate from the strong SOC of $Cr_{1/3}TaS_2$.[18] The strong SOC could also generate large non-adiabatic torque in $Cr_{1/3}TaS_2$ and allow much faster soliton motion at a much smaller current density. Our work clarifies that high-quality $Cr_{1/3}TaS_2$ single crystals are chiral magnets. $Cr_{1/3}(Nb,Ta)S_2$ could serve as an intriguing platform for the flexible engineering of chiral magnetic solitons with tunable SOC.

2. EXPERIMENTAL METHODS

High-quality $Cr_{1/3}TaS_2$ single crystals were grown by chemical vapor transport method. High-purity Cr (99.99%), Ta (99.99%), and S (99.99%) powders were mixed, ground, and sealed in an evacuated quartz tube and then sintered at 750 °C for 48 hours. The resultant powder was then sealed with the I_2 agent in another evacuated quartz tube and kept in a two-zone tube furnace for 200 hours with the hot and cold ends at 1060°C and 950°C, respectively. Afterward, the quartz tube containing $Cr_{1/3}TaS_2$ single crystals was slowly cooled to room temperature by ~ 20 °C per hour. Energy dispersive X-ray (EDX) spectroscopy was measured using a Hitachi 3400N-II Scanning Electron Microscope with the EDX option. X-ray diffraction (XRD) experiments were carried out using a Rigaku Miniflex X-ray spectrometer. X-ray Laue backscattering experiments were performed using a Photonic Science X-ray Laue camera with a rotating anode generator X-ray source. Quantum Design physical property measurement system (QD-PPMS) with a vibrating sample magnetometer (VSM) option was used to measure the magnetic properties. The dc transport option in conjunction with the QD-PPMS was used to measure the longitudinal resistivity (ρ_{xx}) and Hall resistivity (ρ_{xy}). The

electrical transport measurements on the sample were carried out using a conventional 5 probe Hall configuration.

2. RESULTS AND DISCUSSION

3.1. Chemical composition and crystal structure

The $Cr_{1/3}TaS_2$ single crystals are plate-like and hexagonal in shape, with a typical size of 5 mm × 3 mm, as shown in the inset of **Figure 1(a)**. As the ionic ordering and the chiral lattice structure are sensitive to the concentration of intercalated magnetic ions, we verified the chemical composition of our $Cr_{1/3}TaS_2$ single crystals by EDX method. EDX experiments were carried out on 3 different areas of a single crystal, and one of the EDX spectra is shown in Figure 1(a). The chemical composition was estimated by comparing the ratio of the integrated intensity of individual elemental peaks. The average over the 3 different areas results in a composition of $Cr_{0.33(6)}TaS_{1.91(3)}$ which is very close to the ideal composition of $Cr_{1/3}TaS_2$. Slowly cooled parent compound TaS_2 crystalizes into a 2H structure with an ABA-type stacking, in which each Ta atom is surrounded by six S atoms in a trigonal prismatic coordination.[29] In contrast, the after-growth quenching stabilizes an ABC-type stacking of Ta and S layers, inducing a so-called 1T structure in TaS_2.[17,22,24,30–32] As our $Cr_{1/3}TaS_2$ single crystals were slowly cooled from 950 °C to room temperature after growth, the crystal structure of the host TaS_2 is expected to be 2H trigonal prismatic, as shown in **Figure 1(d)**. The intercalated Cr ions are expected to be octahedrally coordinated by sulfur atoms in $Cr_{1/3}TaS_2$ single crystals and order in the (1/3, 1/3, 0) superstructure with a chiral space group of $P6_322$, as shown in Figure 1(d). Each unit cell contains two intercalated Cr ions, where space inversion symmetry is broken between two consecutive Cr ions in the same straight line along the *c*-axis. As the inversion symmetry is broken

only along one chiral *c*-axis, $Cr_{1/3}TaS_2$ can be considered an ideal system for the study of the monoaxial chiral magnet. The 2H structure of the host TaS_2 and the chiral lattice structure of $Cr_{1/3}TaS_2$ have been confirmed by our transmission electron microscopy (TEM) experiments.[33] To further characterize the crystal quality, we performed XRD and X-ray Laue backscattering experiments on a $Cr_{1/3}TaS_2$ single crystal. As depicted in **Figure 1(b)**, the XRD pattern only exhibits strong and sharp (*00l*) Bragg peaks. **Figure 1(c)** illustrates the X-ray Laue pattern in which all the peaks can be indexed by the chiral space group of $P6_322$. The lattice parameters of $Cr_{1/3}TaS_2$ estimated from the XRD and X-ray Laue results are $a = b = 5.752$ Å and $c = 12.283$ Å. Our attempt to refine the crystal structure of $Cr_{1/3}TaS_2$ was unsuccessful, as the synthesized powder samples and the crushed single crystals show highly preferred orientation due to their layered structure. Nevertheless, the *a* lattice parameter of $Cr_{1/3}TaS_2$ is almost the same as that of the 2H TaS_2 ($a = b = 3.314$ Å $\times \sqrt{3} = 5.74$ Å), and the *c* lattice parameter of $Cr_{1/3}TaS_2$ is much larger ($c = 12.097$ Å for 2H TaS_2), strongly indicating the intercalation of Cr ions in $Cr_{1/3}TaS_2$.[29,30]

3.2. Magnetic Properties

The magnetic properties of $Cr_{1/3}TaS_2$ may inherit chirality from the underlying chiral lattice. To reveal the chiral magnetic features of our $Cr_{1/3}TaS_2$ single crystals, we measured the magnetic moment as a function of temperature (μ-T) and a function of magnetic field (μ-$\mu_0 H$). **Figure 2(a)** shows the μ-T curves measured with H // ab plane. At $H = 0.2$ T, an interesting kink is observed at 140 K in the μ-T curve. As the magnetic field increases, the kink shifts to lower temperature and finally disappears at fields above 1.4 T. Above 1.4 T, the μ-T exhibits a typical paramagnetic (PM) – FM transition upon cooling. The kink feature in the μ-T curves and its magnetic-field dependence is similar to that of the CHM order in the monoaxial chiral magnet $Cr_{1/3}NbS_2$.[27,34,35] Our Lorenz

transmission electron microscopy (L-TEM) studies also confirm the CHM order in our $Cr_{1/3}TaS_2$ crystals below 140 K, ruling out the antiferromagnetic order for the kink feature in the μ-T curves.[33] The CHM structure consists of spins that form the helical rotation along the chiral c-axis, as depicted in the inset of Figure 2(a). The CHM ground state results from the competition between FM interaction and asymmetric DM interaction in $Cr_{1/3}TaS_2$. Therefore, the μ-T curves show the PM-CHM transition at low field and PM-FM transition at high field. The CHM to FFM transition is further confirmed by the μ-μ_0H curves measured with H // ab plane, as shown in **Figure 2(b)**. At a temperature lower than 140 K, the magnetic moment increases linearly with an increasing magnetic field, followed by a sudden rise toward a saturated value. This sudden increase of the magnetization has been regarded as indirect evidence of a novel intermediate phase during the incommensurate CHM to commensurate FFM transition.[26–28,35] The intermediate phase, namely the CSL, consists of a periodic array of commensurate domains partitioned by incommensurate chiral twists, as illustrated in the inset of **Figure 2(c)**. As H is increased further, the spatial period of CSL increases and finally goes to infinity at the critical field (H_c). Above H_c, the magnetic structure is forced into the FM state (i.e., FFM) by the magnetic field, and the magnetic moment saturates with a value of $\mu_{sat} \approx 2.73\ \mu_B$/Cr at 2 K, which is very close to the theoretical spin only μ_{eff} (z) for a Cr^{3+} ion. The inverse magnetic susceptibility $1/\chi$ vs T is plotted in the inset of **Figure 2(d)**, and the Curie-Weiss fitting gives the T_{cw} = 143.6 K. The CSL feature is further verified by the analytical fit to the normalized μ-μ_0H curves as seen in Figure 2(c). First, the paramagnetic contributions in μ-μ_0H curves at $T < T_{CHM}$ were subtracted using the μ-μ_0H curve at 150 K. Then the magnetic moment of the subtracted μ-μ_0H curves in Figure 2(b) were normalized by dividing the saturated value μ_{sat}, and the magnetic fields were normalized by dividing the critical field H_c. The normalized curves fall on top of each other and show the

characteristic downward convex shape that has been identified as indirect evidence for the CSL. According to the chiral-Sine Gordon theory for monoaxial chiral helimagnet, the normalized magnetic moment follows the equation of $M = g\mu_B S(\frac{2}{\kappa^2} - \frac{2E}{\kappa^2 K} - 1)$, where $E = E(\kappa)$ and $K = K(\kappa)$ are complete elliptic integrals of the second and first kind respectively with the elliptic modulus κ $(0 \leq \kappa \leq 1)$.[3] The dashed line shown in Figure 2(c) is the numerical simulation of the above equation. All our normalized experimental curves fit well with the simulated curve. This empirical scaling behavior of the μ-$\mu_0 H$ curves further confirms the CSL feature in $Cr_{1/3}TaS_2$ single crystals.

Remarkably, the critical field H_c of $Cr_{1/3}TaS_2$ is 1.46 T at 2 K which is 10 times larger than that of the $Cr_{1/3}NbS_2$. The H_c derived from the chiral-Sine Gordon Hamiltonian follows the equation of $H_c = (\frac{\pi q_0 c}{4})^2 J_z S \sim {D_z}^2/J_z$, where c is the lattice constant along the chiral axis, the wavenumber of the zero-field helimagnetic structure q_0 is given by $q_0 = c^{-1}D_z/J_z$, J_z is the interlayer FM exchange interaction strength, and D_z is the *DM* interaction strength.[3,5,36] The L-TEM results of our $Cr_{1/3}TaS_2$ suggest a q_0 ~ 0.042 $Å^{-1}$ which is 3 times larger than that of the $Cr_{1/3}NbS_2$.[33] Using the experimental values of H_c and q_0, we estimated that the $D_z S^2$ ~ 10.2 K and $J_z S^2$ ~ 18 K for $Cr_{1/3}TaS_2$. For the isostructural $Cr_{1/3}NbS_2$, the reported D_zS^2 is 2.9 K and $J_z S^2$ is 18 K.[3,36] Since the D_z is proportional to SOC strength, the larger D_zS^2 of $Cr_{1/3}TaS_2$ can be attributed to its stronger SOC.[18,26,37] Put differently, the strong SOC of $Cr_{1/3}TaS_2$ results in the large D_z and H_c, giving rise to the robustness of CHM and CSL states. Furthermore, the T_{CHM} of $Cr_{1/3}TaS_2$ is 13 K higher than that of the $Cr_{1/3}NbS_2$. The high T_{CHM} may originate from the enhanced intralayer exchange interaction strength. A theoretical work within the three-dimensional mean field (3dMF) approximation suggested that the analytical expression for

the transition temperature T_{CHM} at zero field is $T_c^{3dMF} = \frac{4J_{xy}+2\sqrt{J_z^2+D_z^2}}{3}S^2$.[35] Using the values of T_{CHM}, J_z, and D_z, we estimated that the intralayer FM exchange interaction $J_{xy}S^2$ is 94.7 K for $Cr_{1/3}TaS_2$. The reported $J_{xy}S^2$ value for $Cr_{1/3}NbS_2$ is ~ 86 K.[35] The expression of the H_c is derived from the simplified chiral-Sine Gordon Hamiltonian in which the spins are assumed to be confined in the *ab* plane. We also measured the μ-T and μ-μ_0H curves along the *c*-axis for our $Cr_{1/3}TaS_2$ single crystal (see **Figure S1** in the supporting information). Along the *c*-axis, $Cr_{1/3}TaS_2$ exhibits a moment of 1.05 μ_B/Cr at 3 T and 2 K, which is much smaller than that of the H // *ab*, suggesting a strong magnetic easy-plane anisotropy. Our estimated J_{xy} >> J_z quantitatively justifies the quasi-2d signature of $Cr_{1/3}TaS_2$: the spins in this crystal are strongly coupled within the *ab* plane and are weakly correlated along the *c*-axis. The strong easy-plane anisotropy and the monoaxial chiral feature of $Cr_{1/3}TaS_2$ also ensure that its magnetic ground state is a 1-dimensional (1d) helical spin twist – the CHM order – rather than a 3-dimensional (3d) spin twist (e.g., Skyrmion lattice).[1,38] With an external magnetic field applied perpendicular to the chiral *c*-axis (H // *ab*), the CHM order will gradually transform into the 1d CSL state instead of the 3d Skyrmion lattice.[1,38]

For the CHM – CSL – FFM transition in the *ab* plane, a significant magnetic hysteresis is observed between ramping-up and ramping-down curves, as can be seen in Figure 2(b). Hysteresis is defined as $\Delta H = H_c$(ramp up) – H_c(ramp down). ΔH obtained from Figure 2(b) is plotted in Figure 2(d) as a function of temperature, and it dramatically increases below 126 K upon cooling. The hysteresis is likely due to different energy barriers for the exit and entry of CSL phase as the field is cycled through the saturation of magnetization.[28] Upon cooling, the difference in the energy barriers

increases, giving rise to the increase of ΔH. The hysteresis is as large as 0.2 T in $Cr_{1/3}TaS_2$ at 2 K, in contrast with the imperceptible hysteresis in $Cr_{1/3}NbS_2$.[27]

3.3. Electrical transport properties

The CSL is a nonlinear array of magnetic soliton kinks, each of which could act as a strong scattering potential for conduction electrons and results in the nontrivial electrical transport properties in $Cr_{1/3}TaS_2$. To characterize the electrical transport properties of $Cr_{1/3}TaS_2$, we measured the temperature and magnetic field dependence of longitudinal resistivity ρ_{xx}. An electric current of 1 mA was applied along the *ab* plane, and ρ_{xx} was measured by the voltage drop along the current direction. The magnetic field was applied either along *ab* plane or *c*-axis. **Figure 3(a)** illustrates the temperature dependence of the resistivity ρ_{xx} with H // I // *ab*. The ρ_{xx} decreases upon cooling, confirming the metallic behavior in $Cr_{1/3}TaS_2$. With increasing magnetic field, the ρ_{xx} decreases suggesting a negative *MR*. The differential $d\rho_{xx}/dT$ is calculated and plotted in **Figure 3(b)**. A sharp peak in $d\rho_{xx}/dT$ is found at 140 K at zero field which agrees with the PM – CHM transition. The peak becomes more pronounced and shifts to lower temperature at 1 T, and it disappears at $H \geq 1.4$ T as seen in the inset of Figure 3(b). Above 1.4 T, $d\rho_{xx}/dT$ exhibits a bump at 128 K corresponding to the PM – FFM transition. For H // *c* (I // *ab*), the mechanism governing the transitions is different from what is observed for *H // ab*. In an external magnetic field applied along *c*-axis, the CHM structure transforms to the chiral conical phase (CCP) with a net ferromagnetic component along *c*-axis.[34,39] As shown in **Figure S2(a)**, a sharp peak is seen in $d\rho_{xx}/dT$ curves at $H < 5$ T for H // *c*, and it corresponds to the transition from PM to CHM/CCP. When the magnetic field along *c*-axis increases further, the magnetic moments of CCP gradually tilt toward the *c*-axis and finally reach the FFM state at a saturated magnetic field (e. g., ~ 4.5 T at 125 K), as can be seen in the μ-$\mu_0 H$ curves for H // *c* in

Figure S1(b). Correspondingly, the sharp peak in dρ_{xx}/dT curves for H // c disappears at $H \geq 5$ T, which is close to the saturated magnetic field at 125 K. Above 5 T, the dρ_{xx}/dT curves only exhibit a broad peak which corresponds to the transition from PM to FFM for H // c.

MR that is defined as $MR = \frac{\rho_{xx}(H) - \rho_{xx}(0)}{\rho_{xx}(0)}\%$, is obtained from the magnetic field dependence of ρ_{xx}, where $\rho_{xx}(0)$ is the longitudinal resistivity at zero field. **Figure 3(c)** depicts the magnetic field dependence of *MR* measured with H // I // ab at various temperatures. Negative *MR* can be seen in the full range of temperatures except at 125 K where a positive kink is observed. This kink coincides with the transition field H_c observed in the μ-$\mu_0 H$ curve at 125 K as shown in **Figure 3(d)**. Above H_c, the *MR* decreases almost linearly with increasing magnetic field, which is the typical behavior of FFM state. At 2 K, the *MR* exhibits a dome shape at low field and then saturates above a transition field H_c. The transition field H_c is consistent with that observed in the μ-$\mu_0 H$ curve, as shown in Figure 3(d). A significant hysteresis of ~ 0.2 T is also observed in the *MR* curve at 2 K. The dome shape in the *MR* below T_{CHM} can be ascribed to the chiral soliton jumps.[40,41] With increasing magnetic field gradually, the chiral solitons jump and result in the alignment of spins in the direction of the field, then the alignment of the spins reduces the resistance, giving rise to the dome-shape negative *MR*. Discrete soliton jumps have been observed in the *MR* results of nanometer-thick flakes of $Cr_{1/3}NbS_2$.[40] The dome-shape *MR* of our bulk $Cr_{1/3}TaS_2$ crystal is a collection of an enormous number of such discrete jumps, and it also indicates a high density of solitons in the bulk $Cr_{1/3}TaS_2$ crystal.

To quantitatively understand the correlations between chiral soliton density and *MR*, we normalized the *MR* with respect to the magnitude of *MR* at H_c for each temperature. The normalized *MR* is defined as *Normalized MR* = $[\rho_{xx}(H) - \rho_{xx}(H_c)]/[\rho_{xx}(0) - \rho_{xx}(H_c)]$. **Figure 3(e)** presents the

normalized *MR* curves in a temperature range from 2K to 125 K. The normalized *MR* curves almost lie on a single curve. The relative soliton density can be defined as $L(0)/L(H)$ where $L(0)$ and $L(H)$ are the spatial periods of the soliton lattice at zero field and a field of H, respectively. $L(0)/L(H)$ can be derived from the simplified chiral-Sine Gordon Hamiltonian and it follows the equation of $\frac{L(0)}{L(H)} = \frac{\pi^2}{4KE}$, where $\frac{H}{H_c} = (\frac{\kappa}{E})^2$. The dashed line shown in Figure 3(e) is the numerical simulation of the relative soliton density. All our normalized experimental *MR* curves show good agreement with the simulated soliton density at low fields. This empirical scaling behavior of the *MR* curves indicates that the *MR* stems from the magnetic scattering of conduction electrons by an array of chiral magnetic solitons. For comparison, we also measured the *MR* with H // c, as shown in **Figure S1(d)** in the supporting material. The dome-shape *MR* is absent, and a negative *MR* is observed in the full temperature range.

Hall resistivity, where *xy* denotes the direction in *ab* plane perpendicular to *xx*, was measured as a function of the magnetic field with H // c. The Hall resistivity of ferromagnets can be empirically written as $\rho_{xy} = R_0\mu_0 H + \mu_0 R_A M$, where $R_0\mu_0 H$ is the ordinary Hall effect (OHE) and $\mu_0 R_A M$ describes the anomalous Hall effect (AHE).[42,43] **Figure 3(f)** shows the magnetic field dependence of ρ_{xy} of $Cr_{1/3}TaS_2$ at different temperatures. At temperatures above 200 K, the OHE dominates so the ρ_{xy} is linear with respect to the magnetic field.[41–43] The positive value of R_0 at 300 K indicates that the charge carriers are *p*-type. At temperatures lower than 200 K, ρ_{xy} dramatically deviates from linear behavior because $Cr_{1/3}TaS_2$ enters the magnetic ordered state and the AHE emerges. Since the AHE coefficient R_A is negative, the decrease of ρ_{xy} is consistent with the increasing trend of M with an increasing magnetic field.[38,44] The AHE can be ascribed to the emergence of CCP. When the magnetic field is applied along the helical axis (H // c), the CHM phase transforms into the CCP with a

net ferromagnetic component along *c*-axis. As the magnetic field increases, the ferromagnetic component along *c*-axis increases, giving rise to the decrease of ρ_{xy}. At a certain saturated field, the cone closes completely and the FFM state is reached (e. g., ~ 4.5 T at 125 K, see **Figure S1(b)** in the supporting information).[38,45–49] Correspondingly, as shown in Figure 3(f), the ρ_{xy} reaches a minimum at the saturated magnetic fields (e. g., ~ 4.5 T at 125 K) which agrees well with the saturated magnetic field shown in Figure S1(b) for *H* // *c*. The low temperature behavior of ρ_{xy} can be understood by taking into account the mean free path *l*.[39,45] At temperatures below 100 K, the longitudinal resistivity decreases fast and the mean free path *l* increases rapidly as temperature is lowered. As the AHE signal scales with $1/l^2$, it diminishes rapidly at temperatures below 100 K, resulting in the OHE dominating the Hall signal at 75 K and 2 K. The temperature dependence of ρ_{xy} is consistent with previously reported results of $Cr_{1/3}NbS_2$.[38]

3.4. Phase diagram

The phase diagrams were constructed from the results of μ-*T* and μ-$\mu_0 H$ shown in **Figure 4(a)** and **Figure 4(b)**. Figure 4(a) and (b) exhibit the phase diagrams obtained from the results measured by ramping the field up and down, respectively. The color scale shows the magnitude of the magnetic moment. Four different regions are observed in both Figure 4(a) and (b), and are labeled as PM, CHM, CSL and FFM. The critical field H_c, that is obtained by taking the magnetic field where the magnetic moment saturates in the *μ-$\mu_0 H$ curves*, separates the CSL and FFM phases. The blue square dots in Figure 4(a) exhibit the temperature dependence of H_c. In order to distinguish the CHM and CSL phase, the second-order differential $d^2\mu/d\mu_0 H^2$ is calculated (see supporting information **Figure S2(b)**). H_L, that is defined as the critical field where $d^2\mu/d\mu_0 H^2$ begins to increase, separates the CHM phase from the CSL phase.[35] The boundary between CHM/CSL and PM is constructed by the

temperature T_{peak} where the kink occurs in the μ-T curves below 1.4 T. Above 1.4 T, the μ-T curves do not exhibit well-defined kinks. Instead, the first-order differential dμ/dT curves exhibit a broad peak corresponding to the transition from PM to FFM. The peak position T_{peak} is obtained by fitting the broad peak and used to separate the PM and FFM phases. As shown in Figure 4(a), CHM phase dominates at a temperature lower than 140 K and at a magnetic field smaller than 1.4 T, and the CSL state emerges as an intermediate phase between the CHM and FFM phase. Moreover, the convergence of H_c and T_{peak} suggests that a possible tri-critical point may exist at a magnetic field range from 1.35 to 1.4 T and temperature around 125 K, as the black arrow shows. Such a tri-critical point in a monoaxial chiral magnet (e.g., $Cr_{1/3}NbS_2$) in the presence of an applied magnetic field perpendicular to the chiral axis has been predicted theoretically.[46,51] The tri-critical point locates at the intersection of PM, CSL and FFM states.[45,50] Recent experimental studies on $Cr_{1/3}NbS_2$ also suggest the existence of a tri-critical point in its magnetic phase diagram.[28,35,52,53] Our $Cr_{1/3}TaS_2$ single crystal could serve as a new platform for the future detailed study of tri-critical behavior in monoaxial chiral magnets.

The phase diagrams constructed solely based on the *MR* data are presented in **Figure 4(c)** and **Figure 4(d)**, where the magnetic field is ramped up and ramped down respectively. The color scale shows the negative *MR* values. Similar to Figure 4(a) and (b), the four distinct regions corresponding to PM, CHM, CSL and FFM phases can be seen. The critical field H_c for the CSL – FFM transition was identified by the peak position of the differential dρ_{xx}/d$\mu_0 H$. Unlike the μ-T curves below 1.4 T, ρ_{xx}-T curves do not exhibit well-defined peaks, as can be seen in Figure 3(a). Instead, a sharp peak is observed in the first-order differential $d\rho_{xx}/d$T, as shown in Figure 3(b). The boundary between PM and CHM was then constructed using the peak position T_{peak} in the $d\rho_{xx}/d$T curves measured up to

1.3 T. Above 1.4 T the sharp peak is not observable, and a broad $d\rho_{xx}/dT$ peak separates the PM and FFM states. The peak position T_{peak} is determined by fitting the broad peaks in the $d\rho_{xx}/dT$ curves (see **Figure S3(a)** in the supporting information). Similar to what is seen in Figure 4(a) and (b), a tri-critical point is also observed within the magnetic field range from 1.35 to 1.4 T and temperature around 125 K as indicated by the black arrow. The H_L, that is defined as the critical field where $d^2MR/d\mu_0H^2$ begins to decrease (see Figure S2(c) and (d)), is used to construct the boundary between the CHM and CSL phases. As shown in Figure 4(c) and (d), the phase diagrams constructed by the electrical transport data exhibit similar features (e. g., similar H_c and H_L values, similar tri-critical point, and similar range of CSL state) to the magnetic phase diagrams. The H_c and H_L values determined from magnetic moment data and *MR* data are consistent, indicating that the conduction process directly couples with the formation of CSL.

4. CONCLUSION

In conclusion, we synthesized high-quality single crystals of $Cr_{1/3}TaS_2$, characterized their magnetic and electrical transport properties, and mapped out the magnetic phase diagram up to 9 T and down to 2 K. $Cr_{1/3}TaS_2$ exhibits the CHM transition near 140 K. The magnetic phase diagrams confirm that the CSL state emerges as an intermediate phase between the CHM and FFM phases. A possible tri-critical point is also observed in the magnetic phase diagram. The conducting electrons interact with the CHM and CSL orders, giving rise to the nontrivial *MR* in $Cr_{1/3}TaS_2$ single crystals. Compared with $Cr_{1/3}NbS_2$, the T_{CHM} of $Cr_{1/3}TaS_2$ single crystal is higher, the H_c of $Cr_{1/3}TaS_2$ is much larger, the extracted *DM* interaction strength D_z is also bigger. The larger H_c and D_z likely originate from the stronger SOC of $Cr_{1/3}TaS_2$.

We have verified that the high-quality $Cr_{1/3}TaS_2$ single crystals are new metallic monoaxial chiral magnets that can host robust chiral magnetic solitons. The isolated chiral magnetic solitons behave like particles which can be annihilated and created by spin polarized current, making them of fundamental interest for *fast logical operations*.[8–10] Recent theoretical results suggested that the chiral soliton motion can reach a velocity of 4200 m/s at a current density of $0.19 \times 10^{12} A/m^2$, whereas the domain wall in ferromagnetic nanowire in order to reach a velocity of 1400 m/s a current density of $22.8 \times 10^{12} A/m^2$ is needed.[9,11] The non-adiabatic torque that arises from the SOC is a key parameter to realize the fast chiral soliton motion.[19] The strong SOC in $Cr_{1/3}TaS_2$ could induce large non-adiabatic torque and enable the fast soliton motion at low current density. $Cr_{1/3}(Nb,Ta)S_2$ could serve as an intriguing platform for the flexible engineering of chiral magnetic solitons with tunable SOC.

SUPPORTING INFORMATION

Supporting Information is available from the Wiley Online Library or from the author.

ACKNOWLEDGEMENTS

D. O, K.G, Y.G and J. Y thank for the support from New Jersey Institute of Technology and Central Michigan University. The work at NJIT was supported by the US Department of Energy under Grant No. DOE: DE- SC0021188. SWC was supported by the DOE under Grant No. DOE: DE-FG02-07ER46382.

REFERENCES

[1] S. Muhlbauer, B. Binz, F. Jonietz, C. Pfleiderer, A. Rosch, A. Neubauer, R. Georgii, P. Boni, *Science* **2009**, *323*, 915.

[2] Y. Togawa, T. Koyama, K. Takayanagi, S. Mori, Y. Kousaka, J. Akimitsu, S. Nishihara, K. Inoue, A. S. Ovchinnikov, J. Kishine, *Physical Review Letters* **2012**, *108*, 107202.

[3] Y. Togawa, Y. Kousaka, K. Inoue, J. I. Kishine, *Journal of the Physical Society of Japan* **2016**, *85*, 112001.

[4] A. Fert, N. Reyren, V. Cros, *Nature Reviews Materials* **2017**, *2*, 17031.

[5] Y. Tokura, N. Nagaosa, *Nature Communications* **2018**, *9*, 3740.

[6] S. W. Cheong, *Npj Quantum Materials* **2019**, *4*, 53.

[7] H. Ishizuka, N. Nagaosa, *Nature Communications* **2020**, *11*, 2986.

[8] V. Laliena, S. Bustingorry, J. Campo, *Scientific Reports* **2020**, *10*, 20430

[9] K. Koumpouras, A. Bergman, O. Eriksson, D. Yudin, *Scientific Reports* **2016**, *6*, 25685.

[10] K. Koumpouras, D. Yudin, C. Adelmann, A. Bergman, O. Eriksson, M. Pereiro, *Journal of Physics Condensed Matter* **2018**, *30*, 375801.

[11] A. Thiaville, Y. Nakatani, J. Miltat, N. Vernier, *Journal of Applied Physics* **2004**, *95*, 7049.

[12] S. Okumura, Y. Kato, Y. Motome, *Journal of the Physical Society of Japan* **2018**, *87*, 033708

[13] R. Aoki, Y. Togawa, S. Ohara, *Physical Review B* **2018**, *97*, 214414.

[14] B. Sipos, A. F. Kusmartseva, A. Akrap, H. Berger, L. Forró, E. Tutǐ, *Nature Materials* **2008**, *7*, 960.

[15] T. Ritschel, J. Trinckauf, K. Koepernik, B. Buchner, M. v Zimmermann, H. Berger, Y. I. Joe, P. Abbamonte, J. Geck, *Nature Physics* **2015**, *11*, 328.

[16] K. T. Law, P. A. Lee, *Proceedings of the National Academy of Sciences of the United States of America* **2017**, *114*, 6996.

[17] Y. Horibe, J. Yang, Y. H. Cho, X. Luo, S. B. Kim, Y. S. Oh, F. T. Huang, T. Asada, M. Tanimura, D. Jeong, S. W. Cheong, *Journal of the American Chemical Society* **2014**, *136*, 8368.

[18] T. Moriya, *Physical Review* **1960**, *120*, 91.

[19] G. Tatara, P. Entel, *Physical Review B - Condensed Matter and Materials Physics* **2008**, *78*, 064429.

[20] S. Fan, I. Manuel, A. Al-Wahish, K. R. O'Neal, K. A. Smith, C. J. Won, J. W. Kim, S. W. Cheong, J. T. Haraldsen, J. L. Musfeldt, *Physical Review B* **2017**, *96*, 205119.

[21] K. T. Ko, K. Kim, S. B. Kim, H. D. Kim, J. Y. Kim, B. I. Min, J. H. Park, F. H. Chang, H. J. Lin, A. Tanaka, S. W. Cheong, *Physical Review Letters* **2011**, *107*, 247201.

[22] S. S. Parkin, R. H. Friend, *Philosophical Magazine B: Physics of Condensed Matter; Statistical Mechanics, Electronic, Optical and Magnetic Properties* **1980**, *41*, 65.

[23] S. S. Parkin, A. R. Beal, *Philosophical Magazine B: Physics of Condensed Matter; Statistical Mechanics, Electronic, Optical and Magnetic Properties* **1980**, *42*, 627.

[24] S. S. P. Parkin, R. H. Friend, *Philosophical Magazine B* **1980**, *41*, 95.

[25] Y. Yamasaki, R. Moriya, M. Arai, S. Masubuchi, S. Pyon, T. Tamegai, K. Ueno, T. Machida, *2d Materials* **2017**, *4*, 041007.

[26] T. Moriya, T. Miyadai, *Solid State Communications* **1982**, *42*, 209.

[27] N. J. Ghimire, M. A. McGuire, D. S. Parker, B. Sipos, S. Tang, J. Q. Yan, B. C. Sales, D. Mandrus, *Physical Review B* **2013**, *87*, 104403.

[28] E. M. Clements, R. Das, L. Li, P. J. Lampen-Kelley, M. H. Phan, V. Keppens, D. Mandrus, H. Srikanth, *Scientific Reports* **2017**, *7*, 6545.

[29] A. Meetsma, G. A. Wiegers, R. J. Haange, J. L. de Boer, *Acta Crystallographica Section C Crystal Structure Communications* **1990**, *46*, 1598.

[30] F. J. di Salvo, G. W. Hull, L. H. Schwartz, J. M. Voorhoeve, J. v. Waszczak, *The Journal of Chemical Physics* **1973**, *59*, 1922.

[31] E. Morosan, H. W. Zandbergen, L. Li, M. Lee, J. G. Checkelsky, M. Heinrich, T. Siegrist, N. P. Ong, R. J. Cava, *Physical Review B - Condensed Matter and Materials Physics* **2007**, *75*, 104401.

[32] L. J. Li, W. J. Lu, Y. Liu, Z. Qu, L. S. Ling, Y. P. Sun, *Physica C: Superconductivity and its Applications* **2013**, *492*, 64.

[33] K. Du, **2021,** unpublished.

[34] Y. Cao, Z. Huang, Y. Yin, H. Xie, B. Liu, W. Wang, C. Zhu, D. Mandrus, L. Wang, W. Huang, *Materials Today Advances* **2020**, *7*, 100080.

[35] K. Tsuruta, M. Mito, H. Deguchi, J. Kishine, Y. Kousaka, J. Akimitsu, K. Inoue, *Physical Review B* **2016**, *93*, 104402.

[36] M. Shinozaki, S. Hoshino, Y. Masaki, J. I. Kishine, Y. Kato, *Journal of the Physical Society of Japan* **2016**, *85*, 074710.

[37] K. V. Shanavas, S. Satpathy, *Physical Review B* **2016**, *93*, 195101.

[38] N. Nagaosa, Y. Tokura, Nature Nanotechnology 2013, 8, 899.

[39] A. C. Bornstein, B. J. Chapman, N. J. Ghimire, D. G. Mandrus, D. S. Parker, M. Lee, *Physical Review B - Condensed Matter and Materials Physics* **2015**, *91*, 184401.

[40] Y. Togawa, Y. Kousaka, S. Nishihara, K. Inoue, J. Akimitsu, A. S. Ovchinnikov, J. Kishine, *Physical Review Letters* **2013**, *111*, 107202.

[41] Y. Togawa, T. Koyama, Y. Nishimori, Y. Matsumoto, S. McVitie, D. McGrouther, R. L. Stamps, Y. Kousaka, J. Akimitsu, S. Nishihara, K. Inoue, I. G. Bostrem, V. E. Sinitsyn, A. S. Ovchinnikov, J. Kishine, *Physical Review B* **2015**, *92*, 220412.

[42] R. Karplus, J. M. Luttinger, *Physical Review* **1954**, *95*, 1154.

[43] C.-X. Liu, S.-C. Zhang, X.-L. Qi, *Annual Review of Condensed Matter Physics* **2016**, *7*, 301.

[44] N. Nagaosa, J. Sinova, S. Onoda, A. H. Macdonald, N. P. Ong, *Reviews of Modern Physics* **2010**, *82*, 1539.

[45] M. Lee, Y. Onose, Y. Tokura, N. P. Ong, *Physical Review B - Condensed Matter and Materials Physics* **2007**, *75*, 172403.

[46] V. Laliena, J. Campo, Y. Kousaka, *Physical Review B* **2016**, *94*, 094439.

[47] Y. Masaki, R. Aoki, Y. Togawa, Y. Kato, *Physical Review B* **2018**, *98*, 100402.

[48] B. J. Chapman, A. C. Bornstein, N. J. Ghimire, D. Mandrus, M. Lee, *Applied Physics Letters* **2014**, *105*, 072405.

[49] J. I. Yonemura, Y. Shimamoto, T. Kida, D. Yoshizawa, Y. Kousaka, S. Nishihara, F. J. T. Goncalves, J. Akimitsu, K. Inoue, M. Hagiwara, Y. Togawa, *Physical Review B* **2017**, *96*, 184423.

[45] M. Arai, Y. Ishikawa, *Journal of the Physical Society of Japan* **1983**, *52*, 1394.

[51] V. Laliena, J. Campo, J. I. Kishine, A. S. Ovchinnikov, Y. Togawa, Y. Kousaka, K. Inoue, *Physical Review B* **2016**, *93*, 134424.

[52] H. Han, L. Zhang, D. Sapkota, N. Hao, L. Ling, H. Du, L. Pi, C. Zhang, D. G. Mandrus, Y. Zhang, *Physical Review B* **2017**, *96*, 094439.

[53] E. M. Clements, R. Das, M. H. Phan, L. Li, V. Keppens, D. Mandrus, M. Osofsky, H. Srikanth, *Physical Review B* **2018**, *97*, 214438.

FIGURES

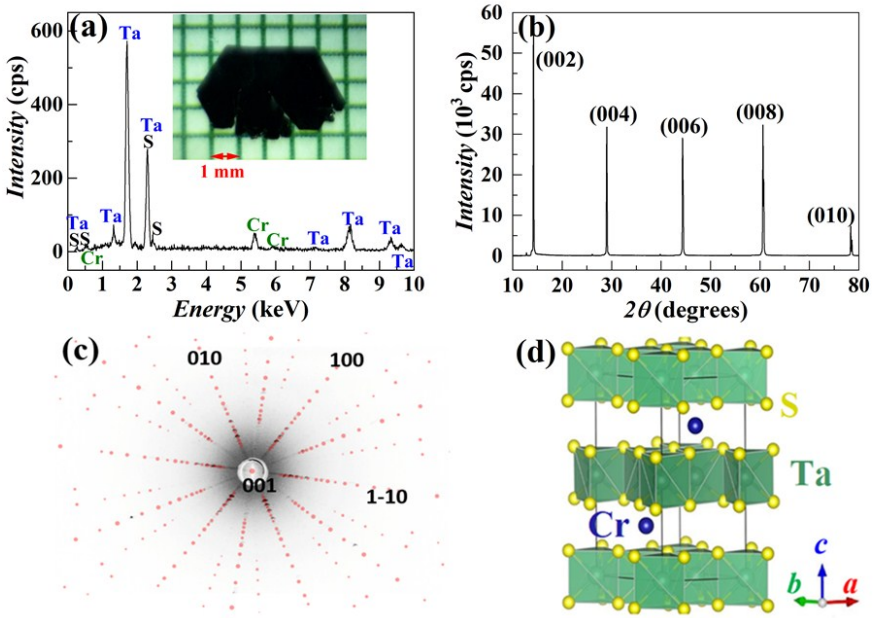

Figure 1: (a) EDX pattern of $Cr_{1/3}TaS_2$. The inset photo shows the hexagonal plate-like crystal. (b) X-ray diffraction pattern of $Cr_{1/3}TaS_2$ single crystal. (c) The X-ray Laue pattern of the $Cr_{1/3}TaS_2$ single crystal. The incident x-ray beam is along the [001] direction. (d) Chiral crystal structure of $Cr_{1/3}TaS_2$. Two Cr ions lie octahedrally coordinated by sulfur atoms between layers of TaS_2.

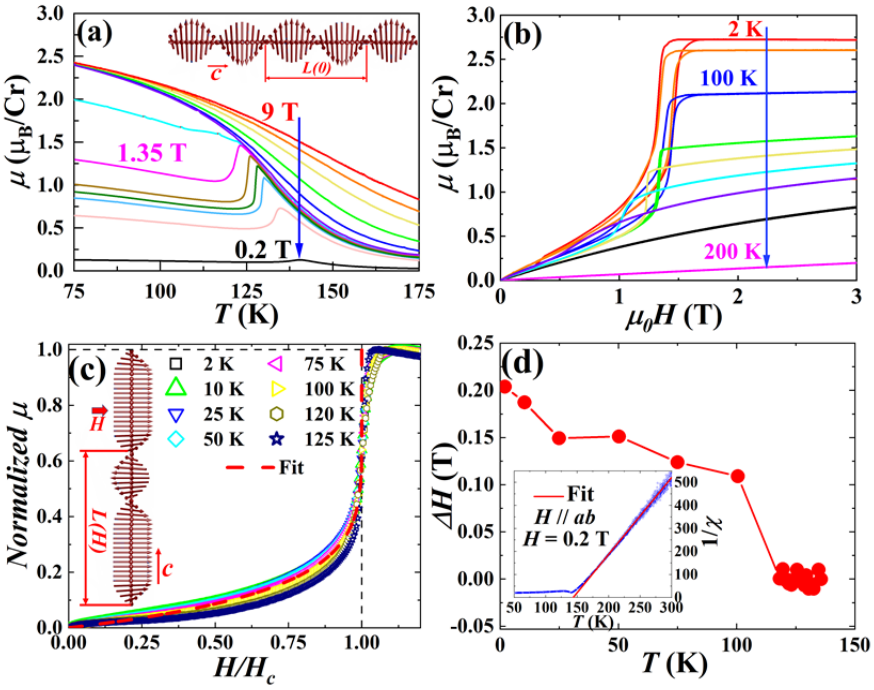

Figure 2: (a) μ-T curves measured with H // ab plane. Inset shows CHM structure with spins that form the helical rotation along the chiral c-axis. (b) μ-μ_0H curves measured with H // ab plane. (c) Normalized μ-μ_0H curves. The inset shows CSL structure under an external magnetic field. (d) ΔH as a function of temperature where ΔH = H_c (ramp up) - H_c (ramp down). The inset shows the temperature dependence of 1/χ and the Curie-Weiss fitting at 0.2 T.

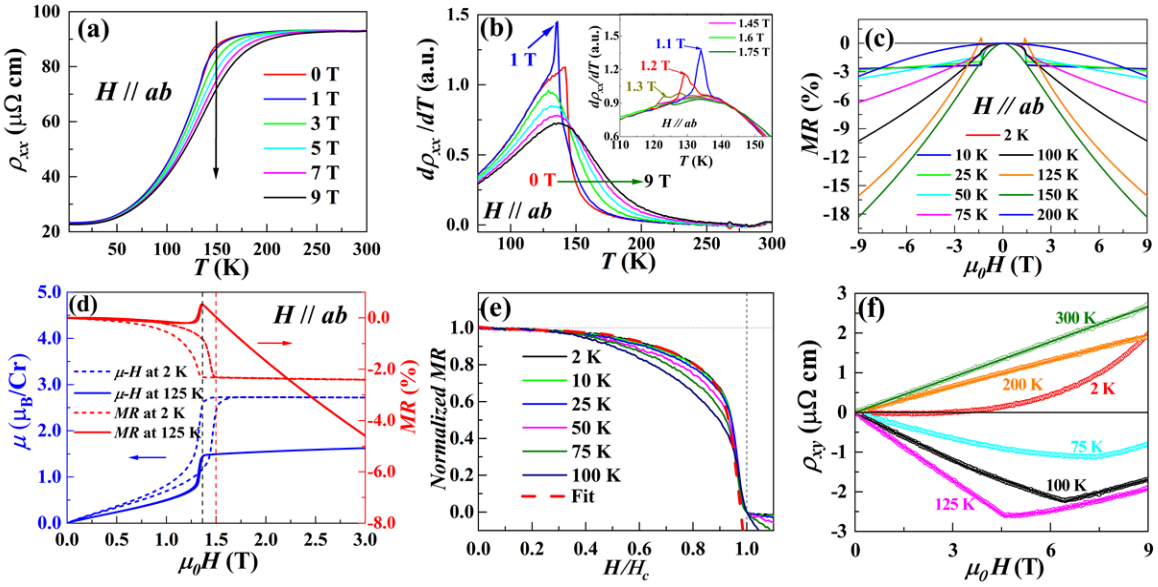

Figure 3: (a) Temperature dependence of resistivity ρ_{xx} at various magnetic fields along H // ab for $Cr_{1/3}TaS_2$. (b) The dρ_{xx}/dT curves at various magnetic fields. The inset shows the dρ_{xx}/dT curves from 1.1 T to 1.75 T measured on a second sample. (c) Magnetic field dependence of MR for $Cr_{1/3}TaS_2$ at various temperatures for H // ab. (d) Comparison between MR and μ-μ_0H curves of $Cr_{1/3}TaS_2$ at 2 K and 125 K for H // ab. (e) Normalized MR curves where the *Normalized MR* = $[\rho_{xx}(H) - \rho_{xx}(H_c)]/[\rho_{xx}(0) - \rho_{xx}(H_c)]$. (f) Magnetic field dependence of Hall resistivity of $Cr_{1/3}TaS_2$ at various temperatures.

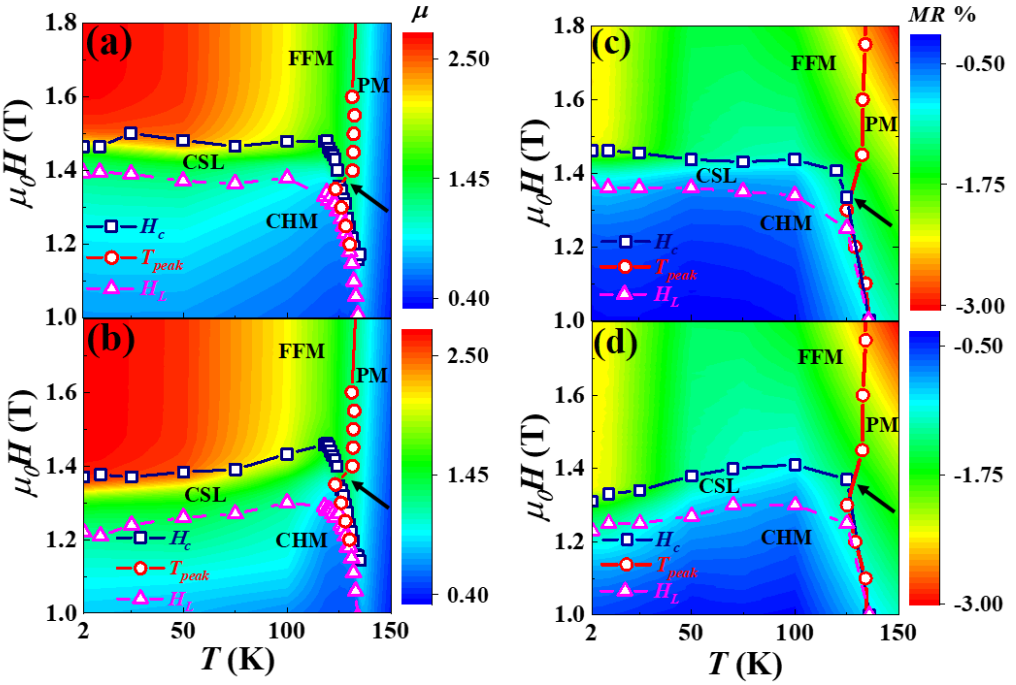

Figure 4: (a) – (b) The magnetic phase diagrams constructed from the results of μ-T and μ-$\mu_0 H$ measured by ramping the field up and down, respectively. The color scale shows the magnitude of the magnetic moment. (c) – (d) The *MR* phase diagrams constructed from the results of ρ_{xx}-T and ρ_{xx}-$\mu_0 H$ measured by ramping the field up and down, respectively. The color scale shows the value of *MR*. The black arrows indicate the possible tri-critical point.

Table of Contents

A new chiral helimagnet $Cr_{1/3}TaS_2$ exhibits the chiral soliton lattice (CSL) under magnetic field. The conducting electrons interact with CSL, resulting in nontrivial magnetoresistance in $Cr_{1/3}TaS_2$. Compared with $Cr_{1/3}NbS_2$, the stronger spin-orbit coupling (SOC) of $Cr_{1/3}TaS_2$ induces larger Dzyaloshinskii-Moriya interaction and more robust CSL. $Cr_{1/3}(Nb,Ta)S_2$ could serve as a platform for flexible engineering of CSL with tunable SOC.

*Dimuthu Obeysekera, Kasun Gamage, Yunpeng Gao, Sang-wook Cheong, Junjie Yang**

The magneto-transport properties of $Cr_{1/3}TaS_2$ with chiral magnetic solitons